

Ab initio study of AlN: Anisotropic thermal expansion, phase diagram, and high-temperature rocksalt to wurtzite phase transition

Steve Schmerler* and Jens Kortus

TU Bergakademie Freiberg, Institute of Theoretical Physics, Leipziger Strasse 23, 09599 Freiberg, Germany

(Received 14 November 2013; revised manuscript received 3 February 2014; published 28 February 2014)

We calculate the anisotropic thermal expansion of wurtzite AlN within the quasiharmonic approximation by sampling the volume as a function of two unit cell axes. From the derived Gibbs energy for the low pressure wurtzite phase and the high pressure rocksalt phase, we calculate the phase diagram. By applying *ab initio* molecular dynamics, we can confirm recent experimental findings regarding a temperature-driven rocksalt to wurtzite backward phase transition. We propose a detailed mechanism for the transition and predict the existence of a β -BeO type high-temperature modification of AlN. Furthermore, we find the *h*-MgO type intermediate structure previously reported for AlN and other compounds which show the wurtzite to rocksalt forward pressure-induced phase transition.

DOI: [10.1103/PhysRevB.89.064109](https://doi.org/10.1103/PhysRevB.89.064109)

PACS number(s): 63.20.dk, 64.70.kg, 65.40.-b, 71.15.Pd

I. INTRODUCTION

AlN is a wide gap semiconductor with many important properties such as high electrical resistivity, high hardness, and thermal conductivity, together with a low thermal expansion rate, which makes it a promising material for high power or optoelectronic applications. Furthermore, it is a key binary compound in the SiAlON system [1,2], which is expected to contain a number of high pressure phases that could be useful in mechanical applications as ultrahard materials.

AlN phases relevant in this work are listed in Table I. At ambient conditions, AlN crystallizes in the low pressure hexagonal wurtzite phase (*wz*-AlN). The metastable zinc blende phase was found under epitaxial conditions [3]. At high pressure, the cubic rocksalt phase (*rs*-AlN) is formed [4,5] and the *wz* \rightarrow *rs* transition mechanism was subject to numerous studies of AlN and other compounds [6–14]. The transition is assumed to proceed via an intermediate structure which can be of hexagonal (*h*-MgO) or tetragonal type and the hexagonal path is predicted to be favored by AlN [10]. It has also been shown that no additional high pressure phases besides *rs* are likely to exist up to very high pressures [6].

In addition to quasistatic high pressure syntheses, recent experiments successfully synthesized *rs*-AlN by using shock wave methods [15]. By exposing these samples to high-temperature conditions at ambient pressure, a backward transformation *rs* \rightarrow *wz* was found [16]. *wz*-AlN is also known to appear in fcc-(Ti,Al)N during annealing [17]. While the majority of previous theoretical studies discuss the pressure-induced transition *wz* \rightarrow *rs*, the high-temperature stability of *rs*-AlN at ambient pressure has yet to be investigated. The aim of this paper is therefore to study the proposed high-*T* phase transition *rs* \rightarrow *wz* in detail. In order to provide a comprehensive theoretical picture of the AlN system in terms of thermodynamic properties and phase stability, we calculate the *wz*-*rs* phase diagram by applying density functional theory methods and compare the result to experimental data and other theoretical works. In order to assess the accuracy of the applied methods, we calculate the small anisotropy in the

per-axis thermal expansion of *wz*-AlN and discuss exchange-correlation effects on the phase diagram and thermodynamic properties. The proposed high-*T* phase transition of *rs*-AlN is then investigated by *ab initio* molecular dynamics in Sec. II D.

II. RESULTS

A. Quasiharmonic approximation

In order to calculate the phase diagram and thermodynamic properties such as the thermal expansion $\alpha_x = 1/x(T)dx/dT$, $x = V, a, b, c$ or the isobaric heat capacity $C_P = -T(\partial^2 G/\partial T^2)_P$, the Gibbs energy $G(T, P)$ needs to be determined. This is done within the quasiharmonic approximation (QHA) [18,19] and involves the calculation of the phonon dispersion at several volumes. At each grid point V , the Gibbs energy $G(V, T, P) = E + F_{\text{vib}}(\omega(V), T) + PV$ is calculated from the total energy E and the vibrational contribution F_{vib} to the free energy, which is calculated using the phonon density of states [18]. A mapping $V(T)$ is constructed by minimization of the Gibbs energy $G(T, P) = \min_V G(V, T, P)$, which provides the optimal lattice parameters, volume, and G for this (T, P) .

Phonon calculations have been performed by applying density functional perturbation theory as implemented in the QUANTUM ESPRESSO package [20] using a plane wave basis set and the projector augmented wave (PAW) method [21]. Exchange and correlation were treated with the local density approximation (LDA), Perdew-Burke-Ernzerhof (PBE), and PBEsol functionals [22–24]. The Brillouin zone was sampled by a $6 \times 6 \times 4$ Monkhorst-Pack grid for *wz*-AlN and a $8 \times 8 \times 8$ grid for *rs*-AlN. In the phonon calculations, the same grids were used and Fourier interpolated to $16 \times 16 \times 12$ and $16 \times 16 \times 16$ grids for *wz* and *rs*. In all calculations, a plane wave cutoff of 80 Ry was used. These settings assure convergence of the total energy <1 meV/atom, pressure <0.02 GPa, and lattice parameters <0.001 Å.

It is known from experiment and calculations [25] that *wz*-AlN shows an anisotropy under pressure at constant T , where the c/a ratio decreases with pressure (increases with volume). Now, varying the volume in the QHA and assuming a monotonic dependence $V(T)$, this would result in an increase

*steve.schmerler@physik.tu-freiberg.de

TABLE I. AlN phases. Primitive cell axes a , b , c (Å) and angles α , β , γ (degrees) are obtained with the PBE functional (see Sec. II A).

Phase	Type	Space group	Atoms	a	b/a	c/a
				α	β	γ
wz	Wurtzite	$P6_3mc$ (186)	4	3.127	1	1.603
				90	90	120
rs	Rocksalt	$Fm\bar{3}m$ (225)	2	2.876	1	1
				60	60	60
hs	h -MgO	$P6_3/mmc$ (194)	4	3.310	1	1.265
				90	90	120
bb	β -BeO	PA_2/mnm (136)	8	3.119	1.707	1.707
				90	90	90

of c/a with T . However, it is known [26–31] that wurtzite-type crystals such as wz -AlN show the opposite behavior, namely, c/a decreases with T ($\alpha_a > \alpha_c$), i.e., the anisotropy in c/a during a volume change caused by P is different from that caused by T . Therefore, using a series of volumes for the QHA, where each unit cell and the atomic positions are relaxed at $T = 0$ (called the “1D” method below) will not result in the experimental c/a - T trend, even if both a and c will of course increase with T . However, note that the anisotropy in the high- T limit [30] is only about $1 \times 10^{-6} \text{ K}^{-1}$ or $\alpha_a/\alpha_c = 1.22$ and therefore the calculated volume expansion $\alpha_V = 2\alpha_a + \alpha_c$ using this method will be sufficiently accurate in most cases. If, however, the behavior of the per-axis thermal expansion is of interest, one needs to sample a and c independently in order to find the correct c/a at each T within the QHA. For the cubic rs -AlN, scaling the a axis is sufficient. A very similar approach has been used before for the study of wz -ZnS [31].

In this paper, we used a grid of 265 (a, c) pairs for wz and 75 a points for rs . The atomic positions of each wz structure were relaxed before the phonon calculation. In case of rs , atoms remain at their Wyckoff position at each volume due to symmetry. The obtained Gibbs energy $G(V, T, P)$ at each (T, P) was fitted to a two-dimensional (2D) polynomial $G(V(a, c)) = \sum_{n,m=0}^5 k_{n,m} a^n c^m$ in case of wz and to a one-dimensional (1D) polynomial $G(V(a)) = \sum_{n=0}^5 k_n a^n$ for rs . The parametrization is used to minimize G to obtain $G(T, P) = \min_V G(V, T, P)$. A plot of $G(V(a, c))$ for wz -AlN is shown in Fig. 1.

We note that the applicability of the QHA is based on the requirement that the structure is dynamically stable at each considered volume (and corresponding T), i.e., no soft phonon modes appear, which determines the upper T limit for the QHA. Since we find imaginary frequencies for rs above large volumes of about $10.5 \text{ Å}^3/\text{atom}$ (see also Fig. 6) which correspond to temperatures well above 2500 K at $P = 0$, we restrict the calculation of the phase diagram and thermodynamic properties to below 2200 K.

B. Phase diagram

Having calculated $G(T, P)$ for both phases of AlN, the phase boundary between wz and rs can be constructed by calculating the intersection line of both surfaces G/atom on a (T, P) grid along P for all T . The calculated phase diagram

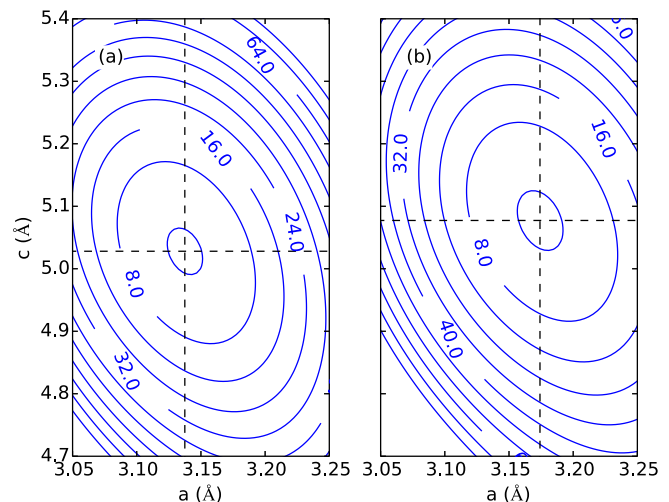


FIG. 1. (Color online) wz -AlN: Contour plot of $\Delta G(V(a, c)) = 0$ –80 meV/atom for (a) $T = 300 \text{ K}$ and (b) 2000 K at $P = 0$. $\Delta G = 0$ minimum points are marked with a cross. They determine the (a, c) pair for the given T and P .

together with experimental points is shown in Fig. 2. We find that the phase boundary calculated using the PBE functional is in good agreement with the experimental data, while the LDA and PBEsol functionals produce a much lower transition pressure, which has been reported before for different systems [33–35]. Our results are also in accordance with another recently published phase diagram [36] (PBE, 1D method), whereas the results of Ref. [37] (LDA, 1D method, transition $> 16 \text{ GPa}$ at 300 K) do not fit into that picture.

Interestingly, the phase boundary calculated using the 1D method is almost the same as the one calculated by explicitly using $V(a, c)$. That is because the c/a anisotropy

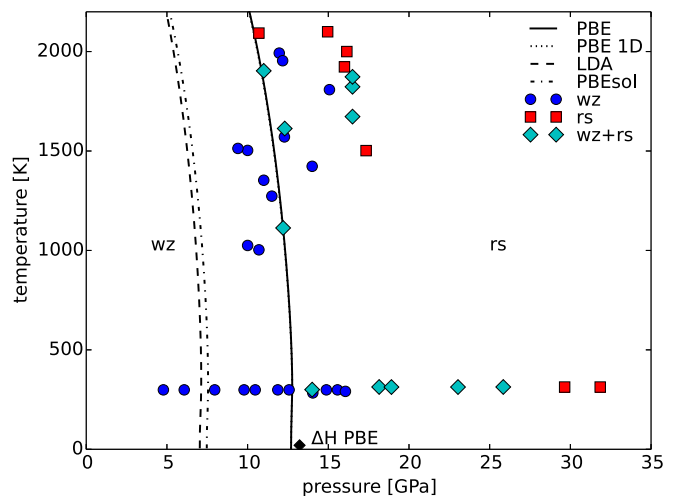


FIG. 2. (Color online) Calculated AlN phase diagram using different functionals. Experimental points from Refs. [2,4,5,32]. $wz + rs$ denotes points of coexistence and 1D the phase boundary calculated using the 1D method for wz (c/a - T trend reversed). The resulting phase boundary lies almost on top of the PBE result. The point labeled ΔH is the phase transition point calculated at $T = 0$ from usual enthalpy $H = E + PV$ differences without zero-point phonon contributions.

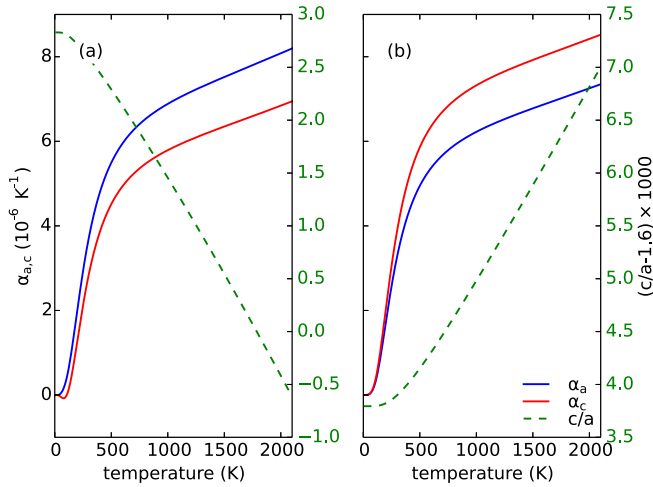


FIG. 3. (Color online) *wz*-AlN: Axis thermal expansion rates and c/a at $P = 0$ using (a) $G(V(a,c))$ and (b) the 1D method. In (a), the c/a ratio decreases with T according to experiment and has an average value of about 1.6.

is small and therefore the mapping $V(T)$ derived in the QHA is essentially not affected, although the $c/a-T$ trend is reversed. The correct c/a behavior, while important for thermal expansion (Sec. II C), may therefore be safely neglected for phase diagrams, as long as the anisotropy is small.

We note that some care must be taken when comparing experimental and calculated transition pressures. The existence of energy barriers along the transition path leads to hysteresis effects, i.e., differences between transition pressures observed during compression (forward) and pressure release (backward), which has been reported for AlN and other compounds [10,33]. At low T , the hysteresis can be such

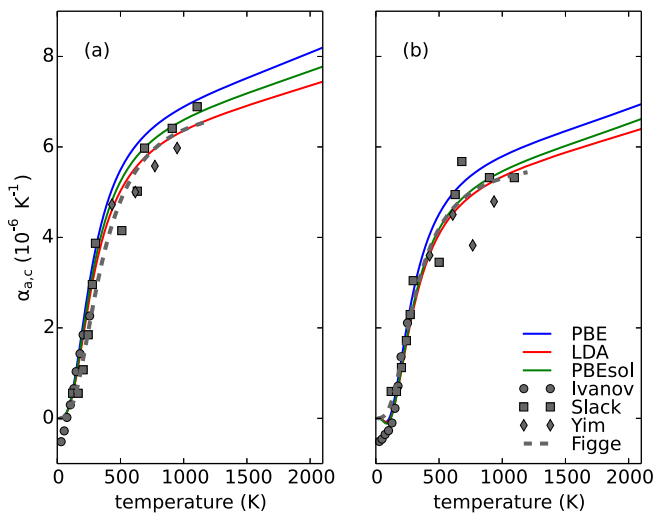


FIG. 4. (Color online) *wz*-AlN: Axis thermal expansion rates (a) α_a and (b) α_c at $P = 0$ compared to experimental data. Solid lines are results from this work, calculated with different functionals. Experimental points from Refs. [26–28,30]. The data from Figge *et al.* [30] is a fit to a Debye model.

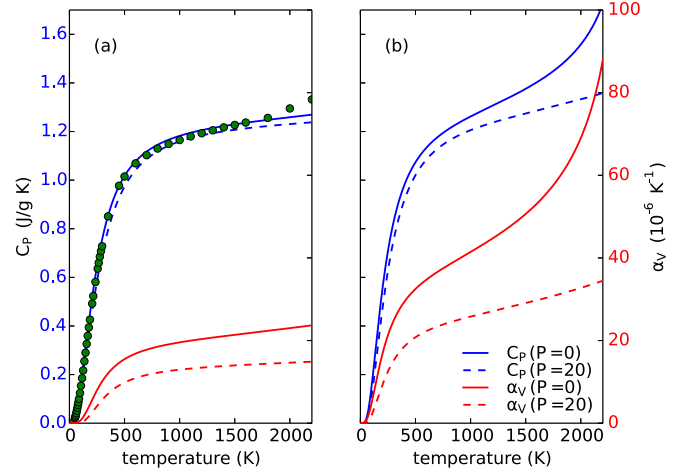


FIG. 5. (Color online) (a) *wz*-AlN and (b) *rs*-AlN: C_p and α_v at $P = 0$ and $P = 20$ GPa. Experimental *wz*- C_p points in (a) at $P = 0$ from Ref. [38].

that the high pressure phase does not transform back even at ambient pressure, which is in fact the case for *rs*-AlN. On the other hand, calculated transition pressures are equilibrium values which do not account for hysteresis and are believed to be located somewhere in the hysteresis window, i.e., experimental forward pressures may be higher than calculated in that case. However, one needs to take the applied exchange-correlation functionals and their trends regarding transition pressures into account. Additionally, high temperatures as well as possibly nonhydrostatic stress conditions in high pressure experiments reduce the hysteresis window, since barriers can be overcome more easily and experimental pressures shift closer to the calculated values. We therefore conclude that our PBE results give a good approximation for the phase boundary

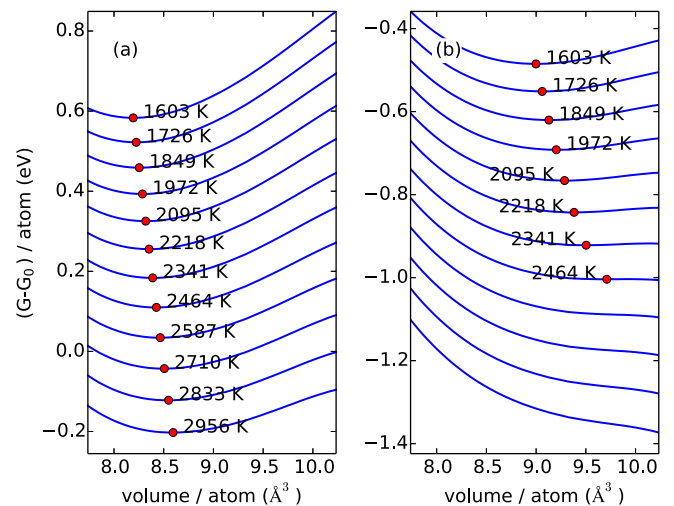


FIG. 6. (Color online) *rs*-AlN: $G(V,T)$ at (a) $P = 20$ GPa and (b) $P = 0$ for $T > 1500$ K. Dots mark the minimum. For volumes bigger than the ones plotted, imaginary frequencies appear (unstable structure, no data evaluation). G is relative to $G_0 = \min_V G(T = 0, P = 0, V)$.

line, especially at high temperatures. Assuming a vanishing hysteresis window at high temperatures would also allow for a back transformation $rs \rightarrow wz$ at low P .

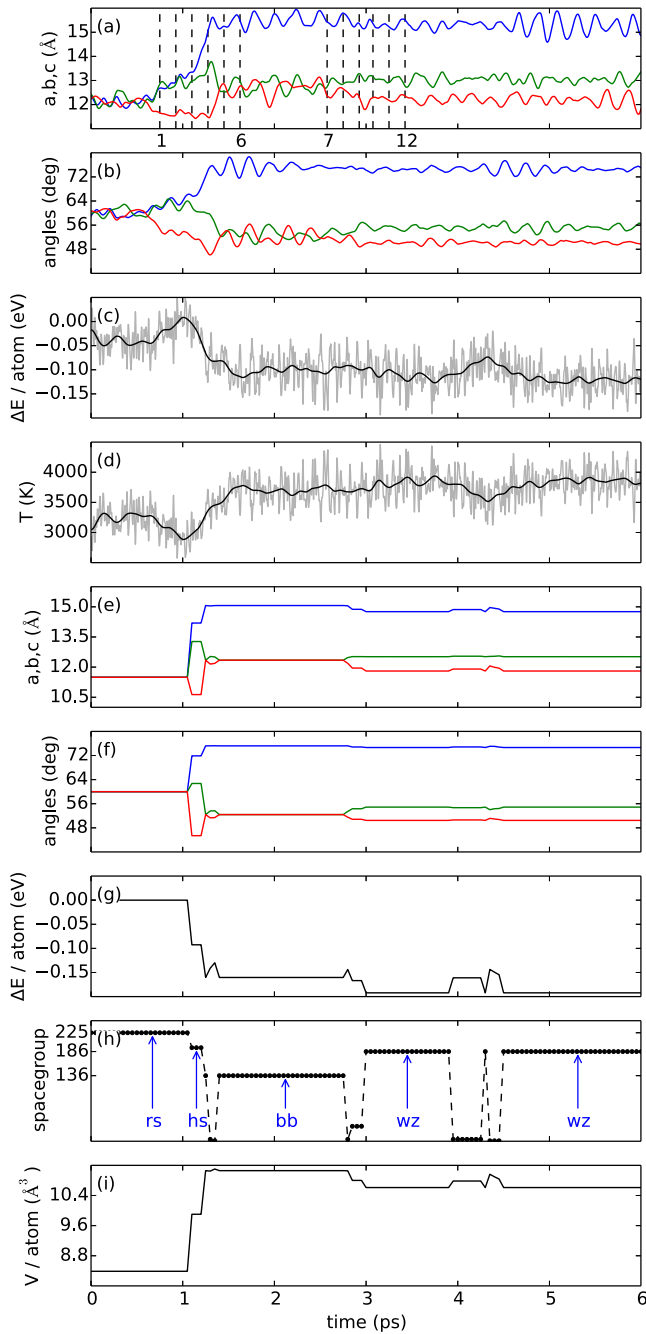


FIG. 7. (Color online) MD trajectory during the phase transition $rs \rightarrow wz$ for a $4 \times 4 \times 4$ supercell of rs -AlN. Vertical lines in the top panel correspond to stage 1 (1–6, Fig. 9) and stage 2 (7–12, Fig. 10). Plotted are cell edges and angles [MD: (a) + (b)]; relaxed: (e) + (f)], total energy relative to transition start [MD: (c)]; relaxed: (g)], (d) temperature, (h) space group number of relaxed structures (see also Table I), and (i) relaxed volume. The time axis is relative to the defined transition start. Note that the cell parameters plotted here reflect changes of the initial rs supercell and should not be confused with the primitive cells of hs , bb , and wz in Table I.

C. Thermodynamic properties

From the QHA-derived $G(T, P)$ and corresponding optimal V , we calculated the thermal expansion and isobaric heat capacity. For wz -AlN, we can reproduce the anisotropic thermal expansion $\alpha_a > \alpha_c$ as shown in Fig. 3. Note the small negative expansion for the c axis at low T , which is due to a negative mode Grüneisen parameter of low-frequency modes [39] below $\sim 400 \text{ cm}^{-1}$ upon expansion of the c axis. A comparison to experimental values is shown in Fig. 4. As can be seen, we get very good agreement for both α_a and α_c for all three functionals. For both axes, LDA produces the lowest expansion rate, followed by PBEsol and PBE, which is known from bulk moduli and lattice parameters where PBE leads to more soft phases (higher α). The LDA and PBEsol results tend to show a better match with some of the experimental data but neither functional performs significantly better in the present case of thermal expansion, whereas we got notably bigger differences in the case of transition pressures.

We also calculated the pressure dependence of the thermal expansion and the isobaric heat capacity C_P for both phases in the range 0–20 GPa, thus crossing the calculated PBE transition pressure of ~ 13 GPa. Results are shown in Fig. 5, where we now plot the volume expansion rate α_V instead of the individual axis rates. For both phases, we find that increasing P leads to a quenching of α as well as C_P , where the latter shows a much smaller sensitivity to P . We find very good agreement with experiment for C_P in the case of wz -AlN. Note that we miss a small contribution at higher T which is due to the fact that we do not include explicit anharmonic effects in our QHA treatment. At high T , the QHA is less reliable since it cannot, by construction, treat anharmonicities other than thermal expansion. If one needs to calculate this contribution, more sophisticated techniques are needed [40].

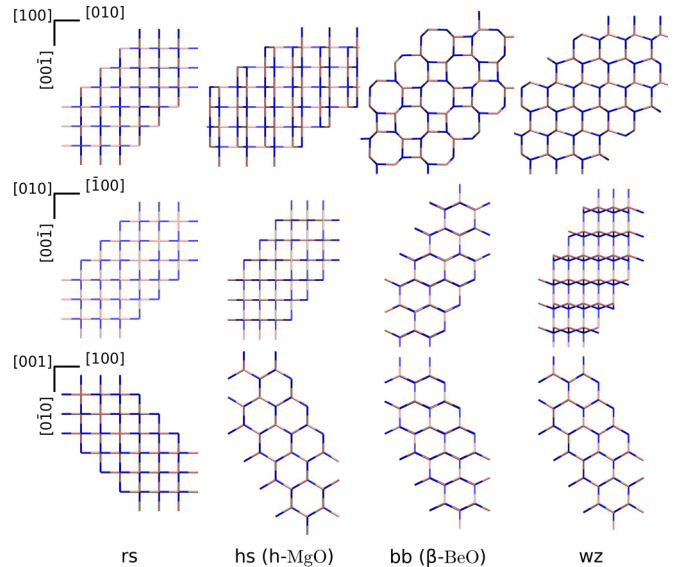


FIG. 8. (Color online) Relaxed structures. For the bb phase we note that similar to β -BeO [42] the 4 atom unit connecting the 8 atom rings (view along $[100]_{rs}$) is not a square but instead shows a slight rhombohedral tilt of 2.45° , which alternates as $ABAB \dots$ along $[001]_{rs}$.

Other sources such as electronic or magnetic contributions are unlikely due to the large band gap and nonmagnetic nature of the phase. Since experimental data are lacking for the rs phase, the calculated values are predictions.

At $P = 20$ GPa where rs -AlN is predicted to be stable according to the calculated phase diagram, C_P and α show their expected high- T behavior. However, at $P = 0$ and temperatures above ~ 1000 K, we find a nonlinear increase in both C_P and α . This can be understood by looking at $G(V)$, from which these properties have been calculated (Fig. 6). At $P = 20$ GPa, a minimum of $G(V)$ can be found up to 3000 K (and above, not shown). The minimum position with respect to T is almost linear, meaning a nearly constant thermal expansion rate, which would be expected in the high- T limit. At $P = 0$ we find a nonlinear increase of the volume and above ~ 2500 K a minimum can no longer be found. That can be interpreted as a signal for a structural instability and shows that rs -AlN is stabilized by P at high T , while it becomes unstable at $P = 0$.

The described behavior of α (and C_P) can be used to define the end of the QHA validity at high T as the point $\partial^2\alpha/\partial T^2 = 0$, where the thermal expansion changes its curvature into nonlinear behavior [41]. Using this definition, we can state that the QHA results for wz and those for rs at $P = 20$ GPa are valid over the whole temperature range, whereas the nonvalid temperature range according to this

definition coincides with that where we expect rs -AlN to be unstable at high temperatures. These considerations are, however, not sufficient criteria for phase stability and one needs to apply other methods in order to investigate the thermal stability.

D. High-temperature phase transition

1. Molecular dynamics

It is in general desirable to observe the proposed $rs \rightarrow wz$ transition directly in molecular dynamics (MD) at the T and P conditions where the transition is expected and without prior assumptions about transition states and a specific transition mechanism. MD is applicable if the transition can be observed within an accessible simulation time (rare events problem) and without overheating the system close to critical points, such as the melting temperature of the simulated system, which is usually much higher compared to experiment due to periodic boundary conditions (suppression of nucleation and growth) and defect-free model crystals.

We applied density functional theory based Born-Oppenheimer molecular dynamics as implemented in the CP2K code using a hybrid plane wave and Gaussian double- ζ (DZVP) basis containing $2s, 2p, 1d$ contracted radial valence functions optimized for condensed phases [43,44], norm-conserving Goedecker-Teter-Hutter (GTH) [45]

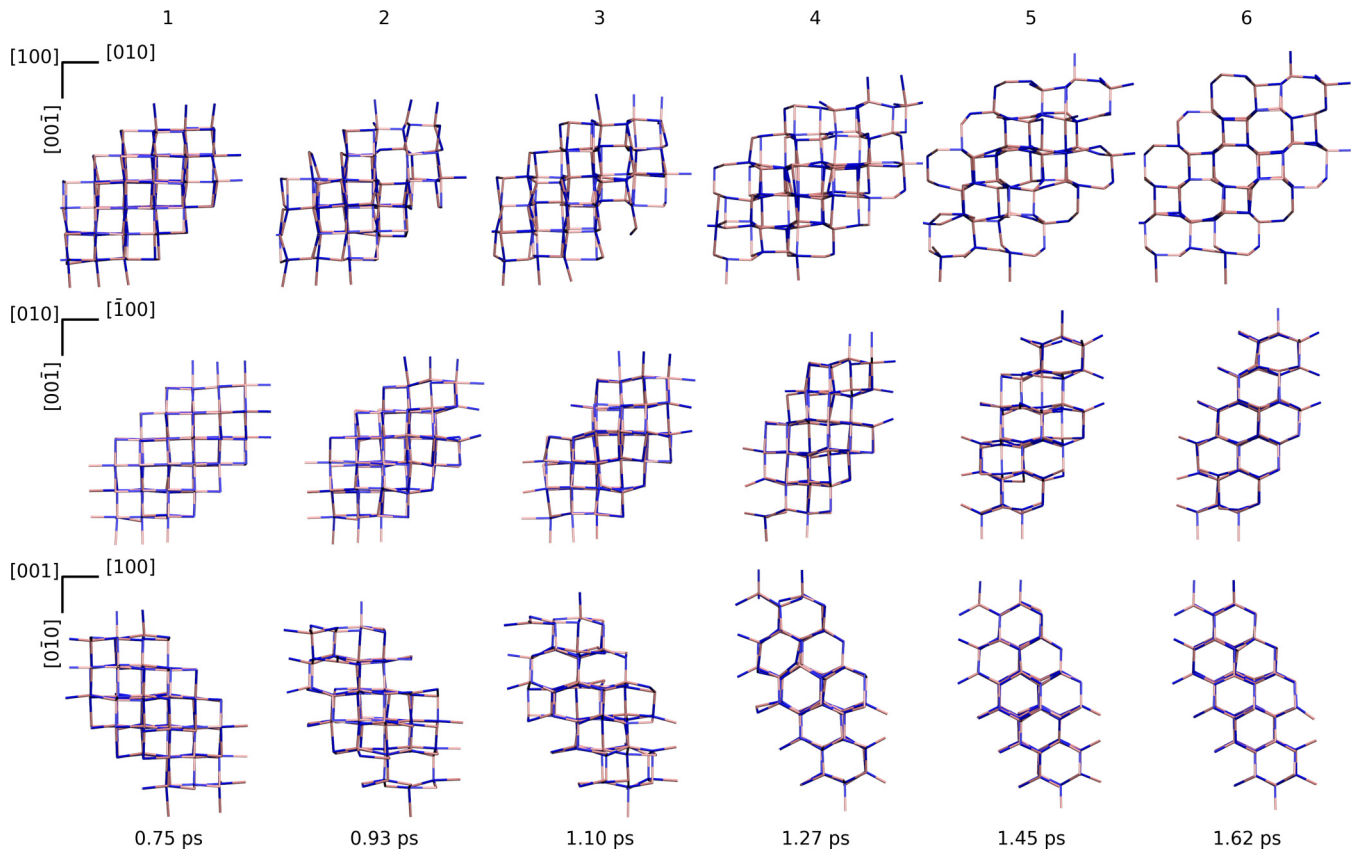


FIG. 9. (Color online) MD snapshots, stage 1. Initial transition from rs (1) to the bb (β -BeO) structure (6) via the hs (h -MgO) intermediate structure (4). Relaxed structures are shown in Fig. 8. Rows denote the view along the respective rs -AlN crystal axis. Note that $[001]_{rs} = [0001]_{wz} = c$ axis of wz . In order to better visualize the transition, the MD trajectory was smoothed by convolution with a Hann window [50] which filters out high-frequency motions while leaving the slower reconstructive atomic and cell movements visible.

pseudopotentials, and a density cutoff of 280 Ry. Exchange and correlation were treated with the PBE functional. Equilibration runs were performed within the NPT ensemble [46], using a Nosé-Hoover thermostat chain [47] for ions and the barostat. Production runs were performed in the NPE ensemble which allows to observe temperature effects during the transition. A time step of 2.5 fs was used and found to provide stable integration. The barostat time constant was set to 200 ps so as to ensure enough coupling between the ionic and cell degrees of freedom (power spectrum overlap) [48].

Several calculations at $P = 0$ and different temperatures were carried out for $4 \times 4 \times 4$ supercells of rs -AlN containing 128 atoms. A phase transition was observed in a number of independent runs at temperatures above 3000 K after 5–150 ps. For those, the calculation was continued for at least 30 ps and then cooled down in steps to below 1500 K. To investigate the structural changes during the transition, MD structures were selected from the trajectory every 0.05 ps and quenched to $T = 0$ by variable cell shape relaxation. For each relaxed structure, the space group was determined. In order to characterize the structures after the transition, structures were relaxed every 1–2 ps to the end of the run.

2. Phase transition mechanism

The phase transition part from a MD run is shown in Fig. 7. The transition itself takes about 3 ps to complete and we separate the process into two stages, in which several transitions transform rs via intermediate structures to wz . The

sequence of intermediates is plotted in Fig. 7(h). Snapshots from the MD in both stages are marked in Fig. 7 by 1–6 and 7–12 which correspond to the structures shown in Figs. 9 and 10. The details of the transformations are explained in the following.

In stage 1, the onset of the transition can be identified as the deviation of all three cell angles from 60° , accompanied by a change in cell axis lengths. Simultaneously we observe a temperature drop, while the potential energy increases by about 0.05 eV/atom (NPE ensemble) and the system obviously crosses an energy barrier. The structure at the total energy peak can be characterized as a stretched rs structure corresponding to structures 2 and 3 in Fig. 9. After having visited this structure, the system undergoes a transition to lower-energy configurations. First, we find a hexagonal intermediate structure of h -MgO (or h -BN) type and $P6_3/mmc$ (194) symmetry, which is represented by structure 4 in Fig. 9. The relaxed structure is shown in Fig. 8. The structure was predicted as an intermediate in ZnO [11] and in AlN along the hexagonal path describing the $wz \rightarrow rs$ pressure-induced transition [10], as well as in MD [8] and metadynamics [12] studies of the $wz \rightarrow rs$ pressure-induced transition in CdSe, where it was termed “honeycomb stacked.” We will refer to it as hs . That structure is then transformed into another intermediate phase (structure 6 in Fig. 9). This tetragonal structure has $P4_2/mnm$ (136) symmetry and is present for about 1.5 ps, which is visible in Fig. 7 as the period between structures 6 and 7, where $b = c$ and $\beta = \gamma$. It is isomorphic to the

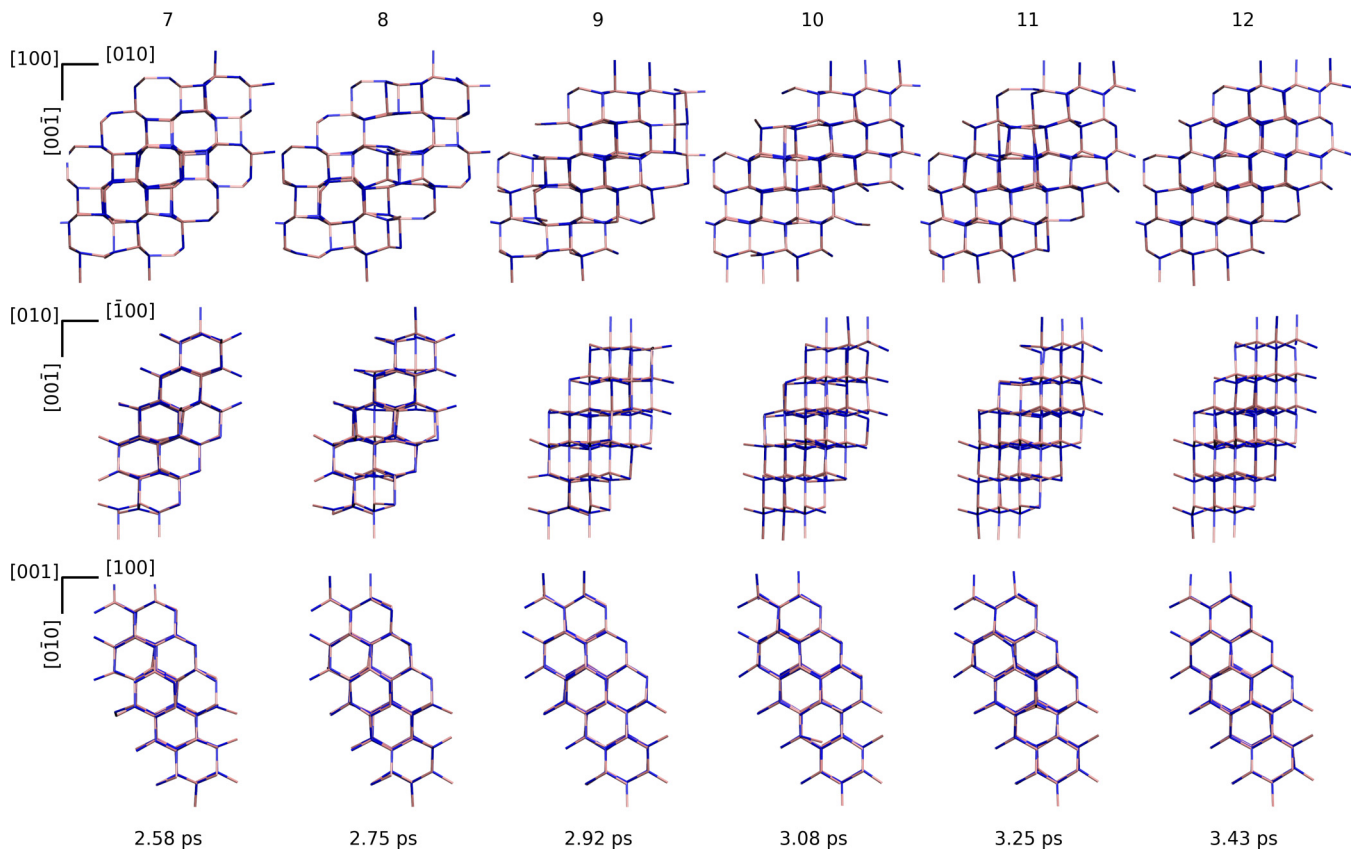


FIG. 10. (Color online) MD snapshots, stage 2. Transition from bb (7) to the wz phase (12). Note how the $[001]_{rs}$ axis remains unchanged during the whole transition.

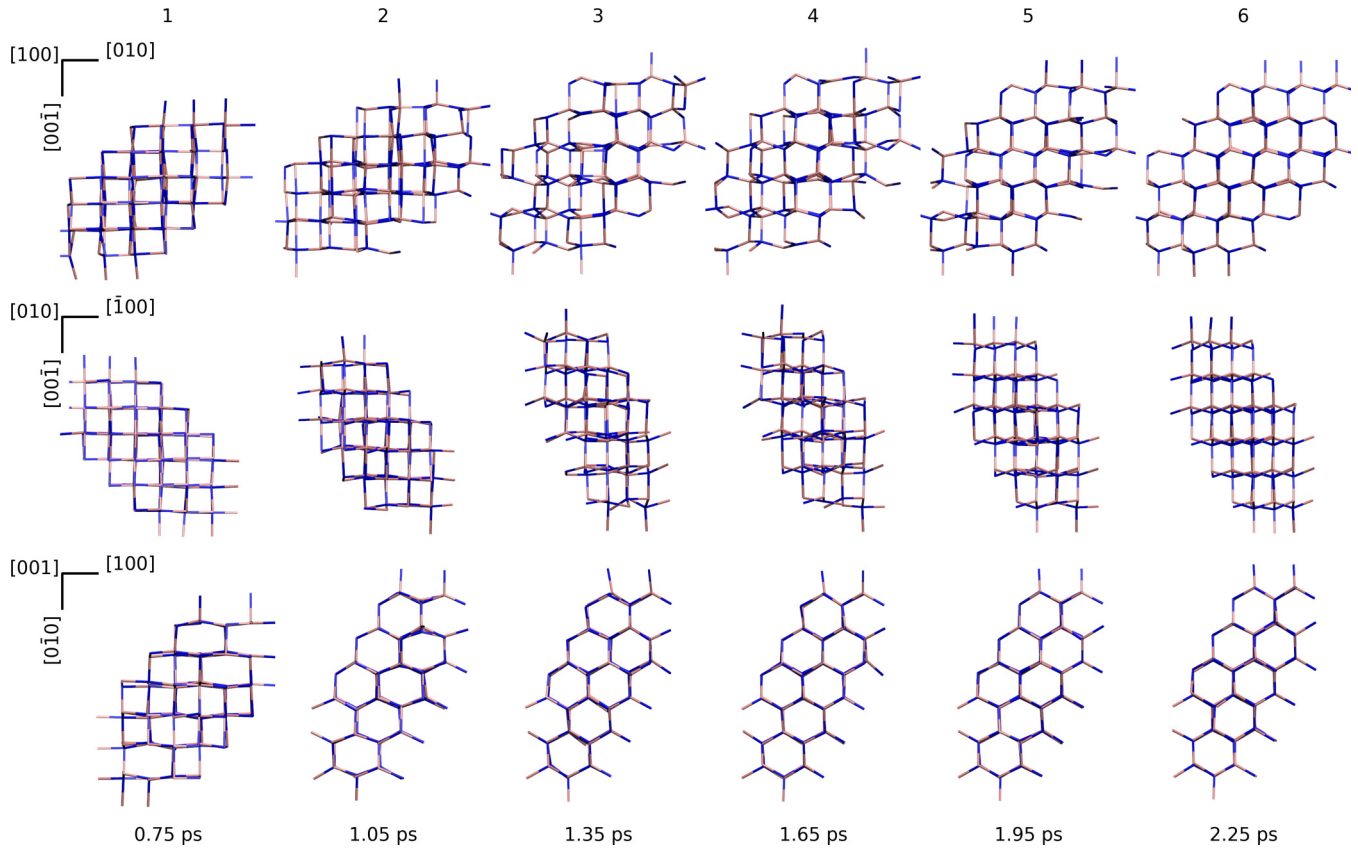


FIG. 11. (Color online) MD snapshots. Direct transition from rs (1) to wz (6) via the hs phase (2) without the occurrence of the bb phase.

high-temperature β -BeO phase [42] and was also found in BN by simulated annealing crystal structure prediction [49]. We will refer to that structure as the bb phase. The relaxed structure is again shown in Fig. 8. In stage 2, the bb phase transforms to wz as shown in Fig. 10. The rearrangements form a hs -like structure (structure 9), which transforms the hexagonal rings of bb along $[010]_{rs}$ to wz type puckered layers.

In some runs we find that bb is not formed as clearly as shown above and the transition proceeds in one stage directly as $rs \rightarrow hs \rightarrow wz$. Snapshots from such a run, performed at the same temperature as the one in Fig. 7, are shown in Fig. 11. Here, we find only one of the relaxed structures during the transition to be characterized as bb . We therefore conclude that the transition via hs is a characteristic feature of the mechanism, whereas the occurrence of the bb phase is not a necessity.

3. Energies of intermediate structures and temperature effects

The relaxed structures capture all essential features of the transition, apart from the total energy peak and stretched rs maximum energy structure. This can be seen in Fig. 7 when comparing the cell edges and angles as well as the energy of MD and relaxed structures. For the energies of the relaxed structures relative to rs [see Fig. 7(g)], we find $hs = -0.092$, $bb = -0.16$, and $wz = -0.192$ eV/atom. Compared to the energy gain of transforming to wz , the bb and wz phases are only separated by about 0.03 eV/atom. Now, due to that small difference and the given temperature, one can expect

that these structures frequently transform into each other. By observing the MD trajectory after the transition some ps after wz has initially formed, we find about 50% of the relaxed structures to be pure wz . The other structures are distorted wz structures or ones which have elements of both the wz and the bb phase with various lower symmetries. We stress that the hs , bb , and wz structures are very similar with regard to the $(001)_{rs}$ plane, which always shows hexagonal rings. After rs transformed to hs and further to bb/wz , this configuration remains stable independently of rearrangements in $(010)_{rs}$ and $(100)_{rs}$. The main temperature-induced distortions which cause either complete or partial $bb \leftrightarrow wz$ transformations [as well as the $hs \rightarrow (bb, wz)$ transition] act along $[001]_{rs}$ by shifting atomic layers relative to each other. These shifts require much less energy compared to a complete $wz \rightarrow rs$ forward transition and therefore occur rather frequently as long as the temperature is not reduced. After cooling the system down, we always recover pure wz structures in all runs where a transition was observed. We note the similarity to BeO, whose high- T form is bb and which also crystallizes in the wz structure at low temperature.

In summary, we can identify two possible transition paths leading from rs to wz , namely, an indirect $rs \rightarrow hs \rightarrow bb \rightarrow wz$ and a direct $rs \rightarrow hs \rightarrow wz$ path, where the latter is in fact an inversion of the hexagonal path. The temperature obviously influences the free energy landscape in a way which allows the formation of the metastable bb intermediate structure. In either case, the transition path eventually leads to the formation of a stable wz phase.

III. CONCLUSION

We have calculated the anisotropic thermal expansion of wz -AlN, which is very small with a difference of only about $1 \times 10^{-6} \text{ K}^{-1}$. Our results compare very well to experimental data, which show that the QHA is a valid approximation and, when combined with *ab initio* methods, a reliable tool for calculating even small differences in thermodynamic properties with high precision, as long as other anharmonic effects play a minor role. From the QHA-derived Gibbs energy, we calculated the wz -AlN– rs -AlN phase diagram and found it to correspond well to experimental data. We investigated exchange-correlation effects and found the phase transition pressure to be much more sensitive to the choice of the functional, whereas structural parameters such as the thermal expansion are less affected. We found indications for a low pressure instability of rs -AlN from the high- T behavior of its thermal expansion and heat capacity. By applying *ab initio* MD, we described the temperature-driven

$rs \rightarrow wz$ transformation mechanism in detail. The transition always forms a h -MgO type intermediate structure and then proceeds either along a reversed hexagonal path or along a modified form of the latter, involving an additional β -BeO type high- T modification. Structural elements of this phase are partly present after the transition in both cases and vanish when the system is cooled down. The obtained results support experimental observations which suggest an instability of rs -AlN at ambient pressure and high- T conditions.

ACKNOWLEDGMENTS

We thank the German Research Foundation (DFG) for funding within the SPP1236 project as well as the ZIH Dresden and the Cluster of Excellence “Structure Design of Novel High-Performance Materials via Atomic Design and Defect Engineering (ADDE)” for providing computing time. Furthermore, we thank J. Neugebauer, M. Schwarz, and K. Keller for fruitful discussions.

-
- [1] T. Ekström and M. Nygren, *J. Am. Ceram. Soc.* **75**, 259 (1992).
- [2] M. Schwarz, M. Antlauf, S. Schmerler, K. Keller, T. Schlothauer, J. Kortus, G. Heide, and E. Kroke, *High Pressure Res.* (2013), doi:10.1080/08957959.2013.857020.
- [3] M. P. Thompson, G. W. Auner, and A. R. Drews, *J. Electron. Mater.* **28**, L17 (1999).
- [4] H. Vollstädt, E. Ito, M. Akaishi, S. Akimoto, and O. Fukunaga, *Proc. Jpn. Acad., Ser. B* **66**, 7 (1990).
- [5] Q. Xia, H. Xia, and A. L. Ruoff, *J. Appl. Phys.* **73**, 8198 (1993).
- [6] J. Serrano, A. Rubio, E. Hernández, A. Muñoz, and A. Mujica, *Phys. Rev. B* **62**, 16612 (2000).
- [7] S. Limpijumngong and S. Jungthawan, *Phys. Rev. B* **70**, 054104 (2004).
- [8] F. Shimojo, S. Kodiyalam, I. Ebbsjö, R. K. Kalia, A. Nakano, and P. Vashishta, *Phys. Rev. B* **70**, 184111 (2004).
- [9] A. M. Saitta and F. Decremps, *Phys. Rev. B* **70**, 035214 (2004).
- [10] J. Cai and N. Chen, *Phys. Rev. B* **75**, 134109 (2007).
- [11] S. E. Boulfelfel and S. Leoni, *Phys. Rev. B* **78**, 125204 (2008).
- [12] C. Bealing, R. Martoňák, and C. Molteni, *J. Chem. Phys.* **130**, 124712 (2009).
- [13] R. F. Zhang and S. Veprek, *Acta Mater.* **57**, 2259 (2009).
- [14] Y. Yao and D. D. Klug, *Phys. Rev. B* **88**, 014113 (2013).
- [15] K. Keller, T. Schlothauer, M. Schwarz, G. Heide, and E. Kroke, *High Pressure Res.* **32**, 23 (2012).
- [16] K. Keller, T. Schlothauer, M. Schwarz, E. Brendler, K. Galonska, G. Heide, and E. Kroke, in *Processing and Properties of Advanced Ceramics and Composites IV*, edited by J. P. Singh, N. P. Bansal, T. Goto, J. Lamon, S. R. Choi, M. M. Mahmoud, and G. Link, Vol. 234 (John Wiley & Sons, Inc., Hoboken, NJ, USA, 2012), pp. 305–311.
- [17] D. Rafaja, C. Wüstefeld, M. Dopita, M. Motylenko, C. Baecht, C. Michotte, and M. Kathrein, *Surf. Coat. Technol.* (2014), doi:10.1016/j.surfcoat.2014.01.039.
- [18] M. T. Dove, *Introduction to Lattice Dynamics* (Cambridge University Press, Cambridge, UK, 1993).
- [19] S. Baroni, P. Giannozzi, and E. Isaev, *Rev. Mineral. Geochem.* **71**, 39 (2010).
- [20] P. Giannozzi *et al.*, *J. Phys.: Condens. Matter* **21**, 395502 (2009).
- [21] G. Kresse and D. Joubert, *Phys. Rev. B* **59**, 1758 (1999).
- [22] J. P. Perdew and A. Zunger, *Phys. Rev. B* **23**, 5048 (1981).
- [23] J. P. Perdew, K. Burke, and M. Ernzerhof, *Phys. Rev. Lett.* **77**, 3865 (1996).
- [24] J. P. Perdew, A. Ruzsinszky, G. I. Csonka, O. A. Vydrov, G. E. Scuseria, L. A. Constantin, X. Zhou, and K. Burke, *Phys. Rev. Lett.* **100**, 136406 (2008).
- [25] F. J. Manjón, D. Errandonea, A. H. Romero, N. Garro, J. Serrano, and M. Kuball, *Phys. Rev. B* **77**, 205204 (2008).
- [26] W. M. Yim and R. J. Paff, *J. Appl. Phys.* **45**, 1456 (1974).
- [27] G. A. Slack and S. F. Bartram, *J. Appl. Phys.* **46**, 89 (1975).
- [28] S. N. Ivanov, P. A. Popov, G. V. Egorov, A. A. Sidorov, B. I. Kornev, L. M. Zhukova, and V. P. Ryabov, *Phys. Solid State* **39**, 81 (1997).
- [29] H. Iwanaga, A. Kunishige, and S. Takeuchi, *J. Mater. Sci.* **35**, 2451 (2000).
- [30] S. Figge, H. Kröncke, D. Hommel, and B. M. Epelbaum, *Appl. Phys. Lett.* **94**, 101915 (2009).
- [31] S. Q. Wang, *Appl. Phys. Lett.* **88**, 061902 (2006).
- [32] L. Bayarjargal and B. Winkler, *Appl. Phys. Lett.* **100**, 021909 (2012).
- [33] A. Mujica, A. Rubio, A. Muñoz, and R. J. Needs, *Rev. Mod. Phys.* **75**, 863 (2003).
- [34] Y. G. Yu, R. M. Wentzcovitch, and R. J. Angel, *J. Geophys. Res.* **115**, B02201 (2010).
- [35] R. G. Hennig, A. Wadehra, K. P. Driver, W. D. Parker, C. J. Umrigar, and J. W. Wilkins, *Phys. Rev. B* **82**, 014101 (2010).
- [36] N. Norrby, H. Lind, G. Parakhonskiy, M. P. Johansson, F. Tasnádi, L. S. Dubrovinsky, N. Dubrovinskaia, I. A. Abrikosov, and M. Odén, *J. Appl. Phys.* **113**, 053515 (2013).
- [37] A. Siegel, K. Parlinski, and U. D. Wdowik, *Phys. Rev. B* **74**, 104116 (2006).
- [38] S. Krukowski, M. Leszczynski, and S. Porowski, in *Properties, Processing and Applications of Gallium Nitride and Related Semiconductors*, edited by J. H. Edgar, S. Strite, I. Akasaki, H. Amano, and C. Wetzel, EMIS Datareviews Series No. 23 (INSPEC, London, 1999), Chap. A1.4, p. 21.
- [39] S. Biernacki and M. Scheffler, *Phys. Rev. Lett.* **63**, 290 (1989).
- [40] B. Grabowski, L. Ismer, T. Hickel, and J. Neugebauer, *Phys. Rev. B* **79**, 134106 (2009).

- [41] P. Carrier, R. Wentzcovitch, and J. Tsuchiya, *Phys. Rev. B* **76**, 064116 (2007).
- [42] D. K. Smith, C. F. Cline, and S. B. Austerman, *Acta Crystallogr.* **18**, 393 (1965).
- [43] J. VandeVondele, M. Krack, F. Mohamed, M. Parrinello, T. Chassaing, and J. Hutter, *Comput. Phys. Commun.* **167**, 103 (2005).
- [44] J. VandeVondele and J. Hutter, *J. Chem. Phys.* **127**, 114105 (2007).
- [45] S. Goedecker, M. Teter, and J. Hutter, *Phys. Rev. B* **54**, 1703 (1996).
- [46] G. J. Martyna, M. E. Tuckerman, D. J. Tobias, and M. L. Klein, *Mol. Phys.* **87**, 1117 (1996).
- [47] G. J. Martyna, M. L. Klein, and M. Tuckerman, *J. Chem. Phys.* **97**, 2635 (1992).
- [48] P. Focher, G. L. Chiarotti, M. Bernasconi, E. Tosatti, and M. Parrinello, *Europhys. Lett.* **26**, 345 (1994).
- [49] K. Doll, J. C. Schön, and M. Jansen, *Phys. Rev. B* **78**, 144110 (2008).
- [50] W. H. Press, S. A. Teukolsky, W. T. Vetterling, and B. P. Flannery, *Numerical Recipes: The Art of Scientific Computing*, 3rd ed. (Cambridge University Press, Cambridge, UK, 2007).